Surfaces and Interfaces 62 (2025) 106179

Contents lists available at ScienceDirect

Surfaces and Interfaces

journal homepage: www.sciencedirect.com/journal/surfaces-and-interfaces

Copper-functionalized hydroxyapatite nanoparticles to counteract fungal infections

Guillermo Escolano-Casado [a], Camilla Fusacchia [b,c], Lorenzo Degli Esposti [b], Margherita Cacaci [d], Damiano Squitieri [d], Francesca Bugli [d,e], Michele Iafisco [b], Lorenzo Mino [a,*]

[a] Department of Chemistry and Interdepartmental NIS Centre, University of Torino, Via P. Giuria 7, 10125 Torino, Italy
[b] Institute of Science, Technology and Sustainability for Ceramics (ISSMC), National Research Council, Via Granarolo 64, 48018 Faenza RA, Italy
[c] Dipartimento di Scienze Matematiche, Fisiche e Informatiche, Università di Parma, Parco Area delle Scienze 7/A, 43124, Parma PR, Italy
[d] Dipartimento di Scienze Biotecnologiche di Base, Cliniche Intensivologiche e Perioperatorie, Università Cattolica del Sacro Cuore, 00168 Roma, Italy
[e] Dipartimento di Scienze di Laboratorio e Infettivologiche, Fondazione Policlinico Universitario A. Gemelli IRCCS, Largo A. Gemelli 8, 00168 Roma, Italy

ARTICLE INFO

Keywords:
Surface functionalization
Copper doping
Antifungal activity
Cytocompatibility
Candidiasis

ABSTRACT

Drug-resistant fungal pathogens pose an increasing threat to human health. Nanoparticles are promising tools for treating and limiting fungal resistance due to their ability to attack microorganisms via multiple mechanisms. In this work, hydroxyapatite (HA) nanoparticles were synthesized and functionalized with copper by ionic exchange at different solution concentrations (from 0.01 to 0.2 M). The physico-chemical properties of the samples were studied using low-temperature N_2 adsorption volumetry, elemental analysis, X-ray diffraction, electron microscopy and IR spectroscopy of adsorbed CO. All the obtained HA particles were poorly crystalline, elongated in the *c*-axis direction, and had a high specific surface area (*ca.* 200 m^2/g). Copper was incorporated into HA surface layers with a Cu^{2+} doping content proportional to the initial concentration, reaching a maximum value of 14 %wt. The antifungal activity of the samples was tested against drug-resistant clinical isolates of *Cryptococcus neoformans* and several *Candida* species strains (*C. parapsilosis, C. krusei, C. tropicalis, C. albicans, C. glabrata, C. auris*). Minimal inhibitory concentrations and fungal growth curves were determined. Cytocompatibility evaluation showed that both undoped and Cu-doped HA samples were not toxic to mammalian cells. The Cu-containing HA samples demonstrated potential as effective and safe antifungal agents with wide-spectrum activity, representing a promising candidate for therapeutic approaches against diverse fungal infections.

1. Introduction

Hydroxyapatites (HAs, $Ca_{10}(PO_4)_6(OH)_2$) are a family of well-known materials extensively present in nature, ranging from mineral rocks to mineralized parts of several living organisms, including fish bones or scales, shells, algae, and mammalians bones, teeth, and antlers [1,2]. Additionally, HA can be synthesized using various methodologies, allowing for tailored characteristics such as different morphologies, surface acid-base properties, degree of crystallinity and particle size [3,4]. Consequently, synthetic HAs are versatile materials used in several fields, including water remediation, heterogeneous catalysis, air purification, and particularly in medical and pharmaceutical applications [5,6].

The structure of stoichiometric HAs (Ca/P ratio equal to 1.67) along their [010] direction is described as a block of stacked layers following the sequence -ABA-ABA-ABA-, with specific composition of $Ca_3(PO_4)_2$ and $Ca_4(PO_4)_2(OH)_2$ for A and B, respectively. Dedicated synthesis methodologies can interrupt this sequence, creating HAs with surfaces enriched in calcium or phosphorous [7–9]. Biomimetic HA NPs consist of a crystalline core embedded in a highly disorder surface layer, providing a high ionic mobility to their surfaces. This allows HAs in aqueous solutions to exchange their constituent ions (Ca^{2+}, $(PO_4)^{3-}$, or OH^-) with ions in the solution [6,10]. The functionalization mechanism, either adsorption or exchange, depends on the characteristics of HA NPs and the nature of the functionalizing species. Literature suggests that poorly crystalline HAs are mainly functionalized by cationic exchange, while, highly crystalline sintered HAs are predominantly functionalized by adsorption [11,12]. Moreover, functionalization by exchange is

* Corresponding author.
E-mail address: lorenzo.mino@unito.it (L. Mino).

https://doi.org/10.1016/j.surfin.2025.106179
Received 12 September 2024; Received in revised form 19 February 2025; Accepted 6 March 2025
Available online 13 March 2025

favored for metal cations with an ionic radius similar to the Ca^{2+} (*ca.* 100 pm) and the same charge [13,14]. Various studies have explored the functionalization and applications of HAs with different cations including M^{2+} (Zn^{2+}, Cu^{2+}, Mg^{2+}, etc.), M^{+} (Ag^{+}, Na^{+}, etc.) and M^{3+} (Tb^{3+}, Eu^{3+}, Sm^{3+}, etc.) [5,15,16].

Fungal pathogens are an increasing problem for human health with *Candida* and *Cryptococcus* species being the most common. *Candida* infections, a global health concern, result from the overgrowth of naturally occurring yeast in the body, leading to various infections [17]. The emergence of drug-resistant strains, such as *Candida auris,* complicates treatment and poses significant health challenges [18,19]. *Cryptococcus* primarily affects individuals with weakened immune systems, like those with HIV/AIDS or undergoing immunosuppressive treatments, with *Cryptococcus neoformans* being the main human pathogen [20]. Traditional treatments for these fungal infections, primarily based on azole compounds, are not always effective, necessitating high doses of antifungal drugs and leading to resistance. For all these reasons, it is important to discover new more effective antifungal treatments [21,22].

Nanoparticles (NPs), due to their tunable properties [23], are considered next generation antimicrobial agents [24]. While their antibacterial properties are well studied, their applications as antifungal agents are less explored [25]. NPs can attack microorganisms through multiple mechanisms potentially hindering the development of antimicrobial resistance. Investigating whether this strategy could also limit fungal resistance development is a promising line of research. The antifungal activity of copper and copper oxide NPs has been previously investigated against various fungi both by themselves or coated with polymers at the surfaces (PVDF. PVC, and PVMK). They have demonstrated a high antifungal response with a relatively low Minimum Inhibitory Concentration (MIC). For instance, biosynthesized copper oxide NPs have been reported to exhibit a minimum inhibitory concentration of 35.5 μg/mL against a not-clinical *C. albicans* strain (ATCC SC5314), using Clinical and Laboratory Standards Institute guidelines [26]. Unfortunately, they also exhibit relatively high cytotoxicity (especially against macrophages), while only the higher concentration tested (39.9 μg/mL) has a hemolytic effect over the 5% (ISO 10993-4 threshold for hemocompatibility). Copper NPs exhibit antimicrobial activity through several mechanisms: (i) copper ions can cause structural damage to the cell membranes of microorganisms, increasing membrane permeability; (ii) copper ions have a high binding affinity with microbial proteins, particularly those containing thiol, imidazole, amino, and carboxyl groups, leading to their deactivation; (iii) copper ions can interact with microbial nucleic acids, inhibiting DNA and RNA synthesis [27,28]; (iv) copper ions can catalyze the production of reactive oxygen species within microbial cells [29]; (v) the introduction of copper ions can disrupt the homeostasis of essential metals within microbial cells [30]. It is also worth noting that for some species, like Candida albicans, Cu availability is crucial for its virulence since it modulates stress responses and enhances antifungal sensitivity under varying copper levels. Notably, Cu can potentiate the effects of azole antifungals like fluconazole, reducing the pathogens tolerance to these drugs [31]. This dual role of Cu, acting both as a nutrient and a potential toxin, highlights its importance in fungal pathogenesis and in treatment strategies against these infections [32].

Given these challenges, in this work copper functionalized HA NPs were prepared, and their antifungal activity was studied. Cu-functionalized HAs may offer advantages over Cu or CuO NPs due to their intrinsic biocompatibility. They have been tested as antibacterial or antimicrobial agents [11,27,33–35], but few studies have focused on their antifungal properties, mainly for agriculture applications [35–40]. Our study aims to obtain HA NPs with nanometric size, low crystallinity degree, and preferentially exposing their {010} facets enriched in phosphorous. Compared with our previous work on Cu-functionalized hydroxypatites [41], we modified the synthesis procedure by operating at room temperature to obtain nanoparticles with higher specific surface area, trying to maximize the final copper content after ion exchange. The chemical composition and structure of the materials was assessed by inductively coupled plasma-optical emission spectrometry, low temperature N_2 adsorption and X-ray powder diffraction. Surface active sites were investigated by Fourier transform infrared spectroscopy of adsorbed probe molecules. The antifungal activity of the Cu-HAs against *Cryptococcus neoformans* and several candida species strains (*C. parapsilosis, C. krusei, C. tropicalis, C. albicans, C. glabrata, C. auris*) was studied with both static-endpoint and kinetic-monitoring approaches. Finally, we tested the biocompatibility of undoped HA NPs and HA NPs doped with the highest Cu concentration (0.1 M) to evaluate the effect of copper release on mammalian cell viability.

2. Materials and methods

2.1. Materials and preparation protocol

Reagents. For the preparation of the undoped HA ammonium hydroxide (NH_4OH, $>$ 85%), calcium acetate ($Ca(CH_3COO)_2 \cdot 0.5\ H_2O$, high purity grade), sodium dihydrogen phosphate (Na_2HPO_4, $>$ 99% anhydrous), and sodium hydroxide (NaOH, $\geq$ 98%) were purchased from Sigma-Aldrich. For the copper incorporation in the HAs, copper nitrate (Sigma-Aldrich $Cu(NO_3)_2 \cdot 2.5\ H_2O$, $\geq$ 99.99%) was used as source of Cu^{2+} ions.

Hydroxyapatite synthesis. Undoped HA (labelled as pristine HA) was prepared by a co-precipitation reaction aimed to produce HA nanocrystals mainly exposing phosphorous-rich terminations at their (010) crystallographic facets [8]. The synthesis temperature was set to 293 K trying to maximize the specific surface area and, thus, the final Cu^{2+} concentration after ion exchange (see below). The methodology is as follows: a Na_2HPO_4 solution (0.35 M, 0.3 L) was dropped over a $Ca(CH_3COO)_2 \cdot 0.5\ H_2O$ solution (0.21 M, 0.3 L) with a rate of 1 drop/-second. The solution containing Ca^{2+} was maintained at pH 10 by adding a NH_4OH aqueous solution (5 M) until complete addition of the $(PO_4)^{3-}$ solution. The obtained dispersion was maturated at room temperature under stirring for 24 h. Subsequently, the HA powder was recovered from the suspension by centrifugation (4500 rpm for 5 min, Jouan BR4i centrifuge), rinsed three times with double distilled water and finally freeze-dried.

As a consequence of the calcium reagent employed ($Ca(CH_3COO)_2$), some acetates remain at the HA surface, acting as complexing agents for Ca^{2+} ions [8,42]. Therefore, the powder was washed twice with a NaOH solution (0.01 M, 0.5 L for 2.5 g) for 5 min at room temperature to remove the calcium-complexing acetates, thus facilitating the subsequent ion exchange procedure.

Copper exchange procedure. Pristine HA powder was sieved isolating the granular fractions having dimensions $<$ 75 μm. To perform the surface substitution of Ca^{2+} by Cu^{2+} ions, 500 mg of the pristine HA powders were suspended in 17 mL of a $Cu(NO_3)_2 \cdot 2.5\ H_2O$ solution at different concentrations (0.01 M, 0.02 M, 0.05 M, 0.1 M, 0.2 M) and stirred for 15 min at room temperature. The pH value was monitored before and after the addition of HA powder, ranging from 4.79 to 3.74 before HA addition and from 6.74 to 3.53 after HA addition, moving from the lowest to the highest copper concentration. Finally, the Cu-containing HA samples were washed and freeze-dried. The five different Cu-containing samples will be referred as: HA-Cu-0.01, HA-Cu-0.02, HA-Cu-0.05, HA-Cu-0.1, and HA-Cu-0.2, where the number refers to the copper concentration in the initial $Cu(NO_3)_2$ solution.

2.2. Characterization techniques

Elemental analysis. The elemental composition of the samples was quantified by Inductively Coupled Plasma-Optical Emission Spectrometry (ICP-OES) by using an Agilent 5100 spectrometer (Agilent Technologies 5100, Santa Clara, CA, USA). The samples were prepared by dissolving 10 mg of the powders in 50 mL of a HNO_3 solution (1 % wt.). The measurements were done in triplicate. Quantification of Ca, P and

Cu content was based on the calibration curves of commercial certified standard solutions (Sigma Aldrich, St. Luis, MO, USA).

Textural properties. Low temperature (77 K) N_2 adsorption volumetry was performed by using an automatic Surface Area and Porosity analyzer (Micrometric ASAP 2020) to evaluate the specific surface area (SSA) of the different materials, calculated by the Brunauer-Emmet-Teller (BET) model and expressed in m^2/g. For the measurement, 100 mg of the powder were activated in dynamic vacuum for 12 h.

X-ray powder diffraction. A general structural characterization of the different samples was performed by X-ray powder diffraction (XRPD) using a PW3050/60 X'Pert Pro powder X-ray diffractometer (Malvern Panalytical, Malvern, UK). XRPD patterns were collected in the Bragg-Brentano geometry using a flat-quartz sample holder. The Cu Kα radiation (1.5406 Å) generated at 40 kV and 45 mA was selected for the collection of the patterns. The 2θ range varied from 10° to 60° with a step size (2θ) of 0.02° and a counting time of 90 s per point. A Rietveld refinement analysis was performed by software TOPAS5, using tabulated HA atomic coordinates as initial input and modeling anisotropic peak-broadening effects by symmetrized spherical harmonics. The unit cell parameters and average sizes of crystalline domains along the hydroxyapatite directions $D_{(002)}$ and $D_{(310)}$ were evaluated from full-profile peak broadening. The instrumental contribution to peak broadening was determined considering the XRPD pattern of a LaB_6 standard sample.

High-resolution transmission electron microscopy. The sample powders were deposited on Cu grids coated with a lacey carbon film. TEM images were obtained with a JEOL 3010-UHR microscope operated at 300 kV of acceleration potential.

Surface analysis. For Fourier Transform Infrared spectroscopy (FTIR) measurements, the HA powder was pressed in self-supporting pellets and then, placed in an IR quartz cell equipped with KBr windows and adapted to perform measurements in transmission mode at low temperatures. Subsequently, the cell was connected to a vacuum line (residual pressure 1×10^{-3} mbar) that permits adsorption-desorption experiment at controlled atmosphere and *in situ* thermal treatments of the sample. Therefore, the self-supporting pellets were activated by a dynamic outgassing treatment at 423 K to remove the water molecules adsorbed at the material surfaces. Afterward, the sample was cooled down by thermal contact with liquid N_2 until *ca.* 100 K before the admittance of 50 mbar of CO that were subsequently outgassed stepwise. The FTIR measurements were carried out in a BRUKER INVENIO R instrument equipped with a MCT detector (resolution = 4 cm^{-1}, zero-filling factor = 4, 64 scans per spectrum). Finally, to make the intensity differences of the FTIR spectra independent of differences in the thickness of the pellets, the datasets were normalized by the optical density (mg of the pellet / area of pellet in cm^2).

2.3. Antifungal assays

Clinical samples. In this study seven different yeast species collected from various clinical samples were used: *Candida albicans, Candida auris, Candida parapsilosis, Candida glabrata, Candida tropicalis, Candida krusei* and *Cryptococcus neoformans*. According to WHO fungal priority pathogens list to guide research, development and public health action [43], three of the selected yeasts belong to the Critical Priority Group *(C. albicans, C. auris* and *C. neoformans),* three belong to the High Priority Group *(C. parapsilosis, C. glabrata* and *C. tropicalis),* and one to the medium priority group *(C. krusei)*. The yeast clinical strains were grown on BD Difco™ Candida BCG Agar (Franklin Lakes, New Jersey, U.S.) for 24 h, incubated at 37 °C and 5% CO_2.

Broth micro-dilution for Minimum Inhibitory Concentration (MIC) determination. To assess antimicrobial efficacy of the HA samples with and without different concentrations of Cu^{2+} ions, a micro-broth dilution experimental set-up was conducted according to EUCAST method for susceptibility testing of yeasts [44]. The used liquid medium for the dilution of inoculum and antifungal compounds was Thermo Scientific™ Sensititre™ YeastONE broth (Waltham, Massachusetts, U.S.), while 96-wells plate used was with round bottom (Corning, New York, U.S.). After 18 h of incubation at 37 °C and 5% CO_2, microbial growth was visually evaluated and was followed by an imaging session to better evaluate yeasts viability. The imaging session was performed with Cytation5 imaging reader (Biotek, Winooski, Vermont, U.S.) on growth aggregates at the bottom of the wells. The protocol set up included the stitching of four contiguous fields (single images with 4 × magnification), and of 20 z-slices to produce a final image with z-projection that covers the entirety of the well and of the growth aggregates (in the z axis).

Growth curves. To evaluate the antimicrobial action of compounds in a dynamic environment, Cytation5 multimode reader was utilized to conduct growth curve experiments. The inoculum and tested drugs were diluted according to the micro-broth dilution for minimal inhibitory concentration (MIC) determination, but the 96-wells plate used was with flat bottom (Corning). To conduct the experiment, the protocol set up included a kinetic protocol of 24 h in which an Optical Density (OD) reading was performed at wavelength equals to 630 nm, every 30 min. The incubation was carried out at 37 °C with 5% CO_2, and the orbital shaking of the multiwell plate was conducted at 150 rpm. The growth curve graphs were designed with GraphPad Prism software version 10.1.2 (La Jolla, California, U.S.).

Cytotoxicity assay. The cytotoxicity evaluation of pristine HA and Ha-Cu-0.1 NPs was assessed with alamarBlue™ Cell Viability Reagent (Thermofisher scientific, Waltham, Massachusetts, U.S.) on VERO E6 monkey (ATCC No. CRL-1586) cell line. The cells were grown and amplified in 25 cm^2 rectangular canted neck cell culture flask (Corning) with Minimum Essential Medium L-Glutammine supplemented (Gibco™, Life technologies, Carlsbad, California, United States) adjusted with 10% Fetal Bovine Serum (Gibco™, Life technologies) and 1% Penicillin/Streptomycin solution (Gibco™, Life technologies). VERO cells at 90% of confluence, evaluated with bright field microscopy, were detached with Trypsin-EDTA 1x (Euroclone, AddLife AB, Stockholm, Sweden) obtained by dilution in Phosphate Buffer Saline (Gibco™, Life technologies). After a 3 min incubation at 37 °C, 5% CO_2 in Steri-cult CO_2 incubator (Thermofisher scientific) with Trypsin/EDTA, cells were completely detached and so, five milliliters of FBS were added to neutralize Trypsin action. Afterwards cells were transferred to 50 mL conical tube (Corning) and centrifugated at 1000 rpm for 10 min with Consul 21R centrifuge (Ortoalresa, Madrid, Spain). Then the obtained pellets were resuspended and counted with NucleoCounter® NC-200™ (Chemometec, Allerød, Denmark). Afterwards, approximately 5×10^4 cells/well were seeded in a 96 wells plate (Corning), treated with HA nanoparticles, and incubated for 24 h at 37 °C and 5% CO_2. Finally, alamarBlue™ Cell Viability (Thermofisher scientific) was performed according to manufacturer instructions. The fluorescence intensity readings were performed with Cytation5 multimode reader with excitation wavelength at 571 nm and emission wavelength of 584 nm. Cell viability percentage was calculated as centesimal fraction of RFU values compared to growth control.

Statistical analysis. All experiments were repeated at least in triplicate, to ensure reproducibility. Broth microdilution data are reported as means without SD, because no differences were detected in replicate MIC values, otherwise data are expressed as means ± SD. Statistical analysis was performed by GraphPad Prism software version 9.3.1 (La Jolla, CA, United States).

3. Results and discussion

3.1. Textural and elemental analysis

The specific surface area (SSA) and the elemental composition of the samples are detailed in Table 1. SSA values for all the samples are around 200 m^2/g, typical for materials with nanometric size [10,45]. Small deviations in SSA between samples fall within the margin of error,

except for the HA-Cu-0.2 sample. Its lower SSA value could be attributed to the acidic pH (3.53) of the $Cu(NO_3)_2$ solution used for the ion exchange procedure. Indeed, the pH did not significantly increase after the HA addition (final pH = 3.74) unlike the other samples. The elemental composition in Table 1 shows a progressive decrease in Ca content paralleled by an increase in Cu content, correlating with Cu^{2+} concentration of ion exchange solution. This indicates copper uptake by the exchanged samples. The maximum amount of Cu^{2+} ions (corresponding to the minimum amount of Ca^{2+} ions) is reached for HA-Cu-0.1, with the difference from HA-Cu-0.2 being negligible. This suggests that the maximum copper uptake for this type of HA is reached at a 0.1 M Cu^{2+} ion concentration, while previous studies on Ca-rich HA samples showed copper exchange saturation at 0.05 M $Cu(NO_3)_2$ solutions [41,46].

Phosphorous content decreases at the highest Cu^{2+} concentrations. To understand this behavior, it is important to highlight that the Ca/P ratio for the pristine HA sample is 1.48, a value which is considerably lower than the stoichiometric HA value of 1.67 [1], indicating a P-rich sample. HAs with Ca/P values lower than 1.67 are more acidic and water soluble. Hence, it is predictable a slight surface dissolution process due to the soaking in the most acidic solutions (highest $[Cu^{2+}]$) [2,6]. However, this process did not significantly affect the measured SSA, except for the HA-Cu-0.2 sample.

The (Ca+Cu)/P ratio of copper-functionalized samples is equal to that of the pristine HA and remains constant at *ca.* 1.48 until HA-Cu-0.02. Then, for higher copper concentrations in solution, it increases reaching 1.62. This suggests that at low Cu concentrations, copper uptake follows a 1:1 ionic exchange, where one Cu^{2+} ion substitutes one Ca^{2+} ion, according to the following mechanism [41]:

$$Cu^{2+}{}_{aq} + 2NO_3{}^{-}{}_{aq} + Ca^{2+}{}_{surf} \rightleftarrows Ca^{2+}{}_{aq} + 2NO_3{}^{-}{}_{aq} + Cu^{2+}{}_{surf}$$

On the other hand, the deviation of (Ca+Cu)/P ratio at higher concentrations implies additional mechanisms, such as surface complexation [11]. This hypothesis is further confirmed by considering the Cu surface density in more concentrated samples, which reaches ~ 7 Cu^{2+} nm^{-2} for the HA-Cu-0.1, exceeding the surface concentration of exchangeable Ca^{2+} ions (~ 5 Ca^{2+} nm^{-2}) [47].

These analyses demonstrate that the copper uptake occurred in all the samples without significantly modifying the HA structure, except for HA-Cu-0.2. Given the similar Cu content of HA-Cu-0.1 and HA-Cu-0.2, the latter will not be included in the following discussion.

3.2. Structural characterization

The structural characterization of the samples was performed by X-ray powder diffraction (XRPD), reported in Fig. 1. The main diffraction peaks present in both pristine HA and Cu-functionalized HAs were indexed as hydroxyapatite single phase (reference pattern JCPDS 00-009-432). This confirms that the Cu exchange procedure did not alter the HA crystal structure. Moreover, XRPD patterns exhibit broad and poorly resolved diffraction peaks, indicating the presence of poorly crystalline HA nanoparticles possessing high SSA.

More detailed structural information was obtained through Rietveld refinement of crystallographic parameters (Table 2). We observed a small contraction of the cell parameters upon Cu doping, ascribed to the smaller ionic radius of Cu^{2+} (73 pm) with respect to Ca^{2+} (99 pm), as already reported in literature [48]. Moreover, for all the samples, the size of the crystalline domains along the [002] direction is considerably larger than along the [310] direction, indicating an elongated morphology, as already reported in previous studies [8,41,49]. The size of the crystalline domains slightly decreases in samples with higher Cu concentration due to the lower pH employed during the synthesis. This results in a slight surface dissolution, as previously discussed.

High-resolution transmission electron microscopy was also employed to further investigate the nanoparticle morphology (Figure S1 in the supplementary materials), considering pristine HA and HA-Cu-0.1, which has the highest Cu content. The HAs NPs show an elongated plate-like morphology and are stacked between them resulting in agglomerates, clearly visible in the low magnification images. In the high magnification images, we can observe interference fringes demonstrating the crystalline nature of the NPs. However, these fringe patterns are interrupted close to the borders of the NPs, where a thin layer (*ca.* 2 nm) of amorphous nature can be appreciated, already described in previous literature [10,50]. No significant differences are observed between the pristine HA and HA-Cu-0.1 samples, in agreement

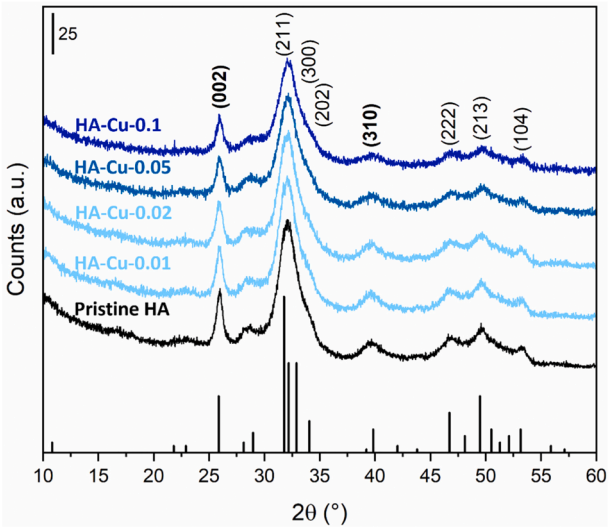

Fig. 1. X-ray diffraction patterns of the pristine HA and the copper-functionalized HAs with the principal diffraction peaks indexed. The pattern of hydroxyapatite reference (JCPDS 9–432) is reported at the bottom.

Table 2
Unit cell parameters and dimension of the crystalline domains along the [002] and [310] directions for the pristine HA and copper-functionalized HA samples.

Sample	a (Å)	c (Å)	$D_{[002]}$ (nm)	$D_{[310]}$ (nm)
Pristine HA	9.469 ± 0.005	6.894 ± 0.005	13.2 ± 0.5	4.4 ± 0.7
HA-Cu-0.01	9.459 ± 0.005	6.887 ± 0.005	12.1 ± 0.6	5.0 ± 0.8
HA-Cu-0.02	9.458 ± 0.005	6.884 ± 0.005	11.1 ± 0.5	4.7 ± 1.0
HA-Cu-0.05	9.435 ± 0.005	6.864 ± 0.005	11.2 ± 0.5	3.9 ± 0.8
HA-Cu-0.1	9.444 ± 0.005	6.871 ± 0.005	10.1 ± 0.5	3.2 ± 0.6

Table 1
Sample codes, BET specific surface area (SSA_{BET}), element weight percent (% wt) composition measured by ICP-OES, and atomic ratios for each sample.

Sample	SSA_{BET} (m^2/g)	ICP-OES			
		$[Ca^{2+}]$ (% wt)	$[Cu^{2+}]$ (% wt)	[P] (% wt)	(Ca + Cu)/P
Pristine HA	199	33.2 ± 0.1	–	17.3 ± 0.1	1.48 ± 0.01
HA-Cu-0.01	219	31.9 ± 0.3	2.6 ± 0.1	17.4 ± 0.1	1.49 ± 0.01
HA-Cu-0.02	210	30.4 ± 0.4	4.1 ± 0.1	17.1 ± 0.2	1.49 ± 0.01
HA-Cu-0.05	205	25.8 ± 0.1	10.8 ± 0.1	16.5 ± 0.2	1.52 ± 0.01
HA-Cu-0.1	192	23.3 ± 0.2	14.0 ± 0.2	15.4 ± 0.1	1.62 ± 0.01
HA-Cu-0.2	170	23.5 ± 0.4	14.7 ± 0.2	15.7 ± 0.3	1.61 ± 0.01

with the XRD results.

3.3. Surface characterization

Fourier Transform Infrared (FTIR) spectroscopy using probe molecules was employed to perform a detailed characterization of the HA surface sites. Carbon monoxide (CO) was selected as probe molecule since it can probe all the cationic sites of interest (Ca^{2+}, Cu^{2+}, Cu^{+}) [51].

Before the FTIR measurements, the samples were outgassed at 423 K to remove the physisorbed water, allowing the adsorption of the CO probe molecules. These activation conditions are a compromise between eliminating the adsorbed water molecules and preserving the structural integrity of the HAs, as previously investigated in detail [8]. Figure S2 reports the full Mid-IR range for the pristine HA and HA-Cu-0.1 samples.

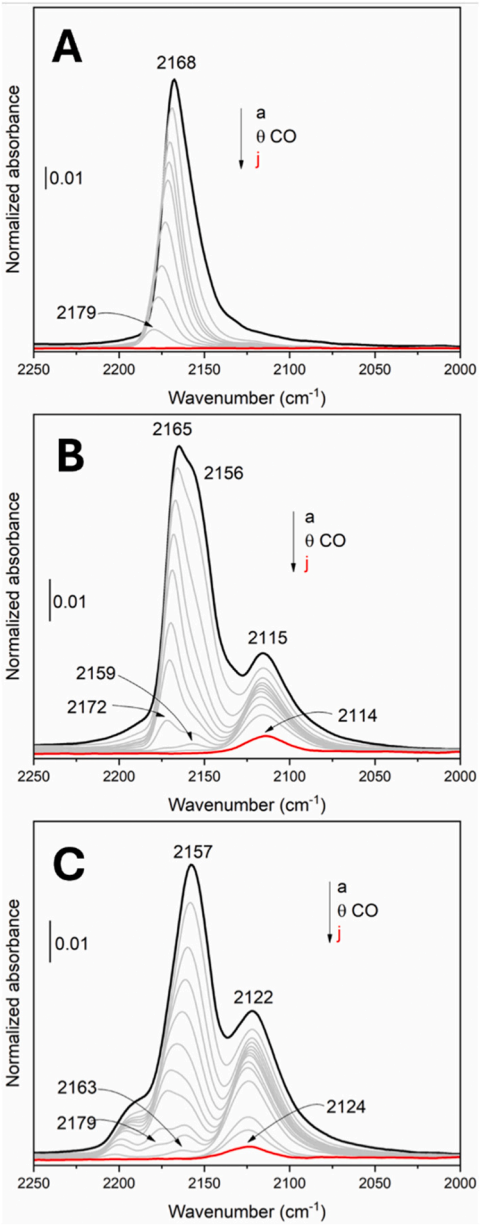

Fig. 2. FTIR spectra of CO adsorbed at low temperature (*ca.* 100 K) on pristine HA (panel A), HA-Cu-0.01 (panel B), HA-Cu-0.1 (panel C), collected at decreasing CO coverages starting from 50 mbar (curves a in black) and stepwise outgassed until 1×10^{-3} mbar (curves j in red). The spectrum of the material after activation has been subtracted from all spectra (see Figure S2 in the supplementary materials for further details).

We can note that the spectral profile is not significantly modified upon Cu functionalization. Moreover, we have further confirmation of the integrity of the HA crystalline structure from the presence in both samples of the sharp peak at 3570 cm^{-1}, ascribed to bulk columnar OH in 4e lattice position [8].

Fig. 2 shows the spectra of CO adsorbed at low temperature (*ca.* 100 K) at decreasing coverages on three representative samples. In the pristine HA (Fig. 2A), the spectrum is dominated by a band centered at 2168 cm^{-1}, which progressively shifts to 2179 cm^{-1}, since the CO–CO interactions decrease at lower coverage [45,52]. This band can be assigned to CO adsorbed on Ca^{2+} ions [7,8,41]. For HA-Cu-0.01 (Fig. 2B), which represent samples with low Cu content, three bands are present: (i) the peak located at 2165 cm^{-1} at maximum CO coverage, attributed to the CO–Ca^{2+}interaction; (ii) the shoulder centered at 2156 cm^{-1} and shifting to 2159 cm^{-1}, due to CO adsorption on Cu^{2+} sites; and (iii) the peak centered at 2115 cm^{-1}, assigned to CO interacting with Cu^{+} cations, whose intensity can vary depending on the specific activation conditions [41,51,53]. Finally, in the spectrum of HA-Cu-0.1 (Fig. 2C), representing samples with high Cu content, the same three bands discussed for the HA-Cu-0.01 can be observed. In this case the intensity of the Cu^{2+} and Cu^{+} signals is higher, in agreement with the higher Cu content, but the Ca–CO interaction band is still visible, indicating that the surface Ca has not been completely substituted with Cu cations.

3.4. Antifungal activity

Fig. 3 shows a selection of images of visible yeasts growth at the round bottom of the multi-well plates used for broth micro-dilution experiments, as detailed in the experimental section. The MIC values determined from these experiments are summarized in Table 3. *C. albicans, C. auris*, and *C. neoformans* are life-threatening microorganisms for immunocompromised patients and are classified as critical priority pathogens on the WHO list of priority fungi. These yeasts, particularly *C. auris*, have a significant multidrug-resistant proportion among healthcare-associated infections [54]. HA-Cu-0.1 and HA-Cu-0.05 samples demonstrate significant antifungal activity against these three yeasts, with MICs ranging from 16 to 32 μg/mL (Table 3). However, HA-Cu-0.05 exhibits a MIC of 64 μg/mL against *C. neoformans*. Kinetic growth curve experiments reflect the static broth microdilution results for *C. albicans* and *C. auris*. In contrast, *C. neoformans* responds uniquely to treatments when the assay is conducted kinetically. As shown in Fig. 4, *Cryptococcus* treated with 0.5 × MIC concentrations of both HA-Cu-0.1 and HA-Cu-0.01 exhibits a nearly halved final optical density (OD) value, approximately 0.34 ± 0.05 after 24 h of incubation (growth control has a mean final OD value of 0.665 ± 0.008). A similar trend is observed with *C. auris* when treated with 0.5 × MIC samples: the final OD values are nearly halved compared to control, but the curve remains in an exponential growth phase, while *Cryptococcus* reached the stationary phase.

C. parapsilosis, C. glabrata, and *C. tropicalis* are major representatives of the non-*Candida albicans* Candida species group (NCAC) and are classified as high-priority pathogens on the WHO fungal priority pathogens list. These *Candida* species, particularly *C. parapsilosis*, exhibit greater resistance to the tested compounds, with the lowest MIC values around 64 μg/mL for *C. glabrata* and *C. tropicalis*. Both *C. parapsilosis* and *C. glabrata* do not show a dose-dependent antifungal effect relative to copper concentration in the HA-Cu samples. Additionally, pristine HA without copper surprisingly inhibits *C. parapsilosis* at high concentrations (128 μg/mL), contrasting with other yeast species, for which MICs are equal to or greater than 256 μg/mL. Kinetic growth curves align with the static broth microdilution results (Table 3). Finally, *C. krusei* is classified as a medium-priority pathogen on the WHO fungal priority pathogens list. A unique characteristic of this *Candida* species is its inherent resistance to azole-based antifungal drugs, severely limiting available treatment options [55]. Among the tested yeast species and compounds, HA-Cu-0.1 and HA-Cu-0.05 exhibited the lowest MICs of 8

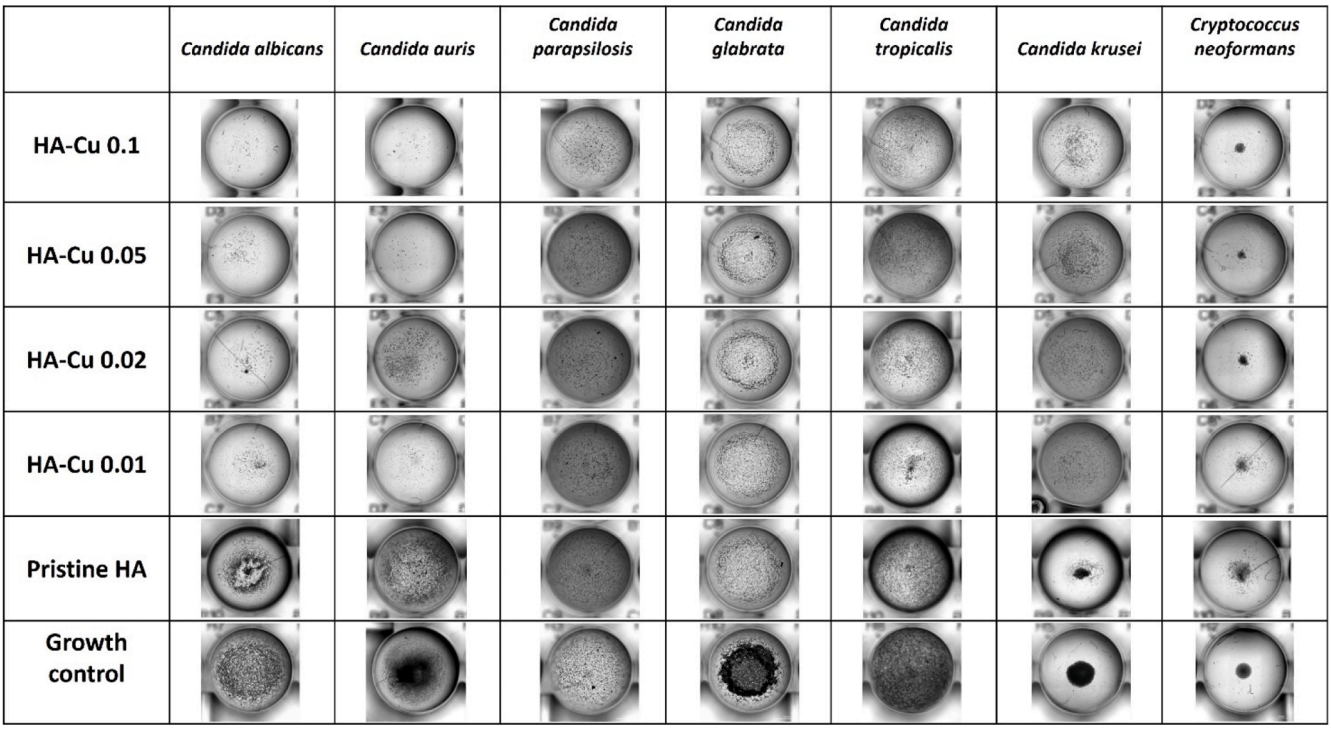

Fig. 3. Images showing visible yeasts growth at the round bottom of the multi-well used for broth micro-dilution experiments. The wells depicted contained the MIC of tested samples ranging from 8 to 256 μg/mL. For experimental conditions where MIC values exceed 256 μg/mL (exclusively for pristine HA), images in this figure represent the maximum tested concentration of the compound (256 μg/mL).

Table 3
MIC values, expressed in μg/mL, and determined by broth microdilution method according to EUCAST guidelines.

Sample	Fungal species						
	C. parapsilosis	*C. krusei*	*C. tropicalis*	*C. albicans*	*C. glabrata*	*C. auris*	*Cryptococcus neoformans*
Pristine HA	128	256	≥ 256	≥ 256	≥ 256	≥ 256	128
HA-Cu-0.01	128	32	128	128	128	64	64
HA-Cu-0.02	128	32	128	64	128	32	64
HA-Cu-0.05	128	8	64	32	64	16	64
HA-Cu-0.1	128	8	64	32	128	16	32

μg/mL against *C. krusei*. *C. krusei* demonstrates a clear dose-dependent susceptibility to HA-Cu, with no significant differences between static and kinetic environments.

Concerning the mechanism of action of Cu doped HA, as mentioned in the introduction, several factors should be considered. However, literature studies involving *Candida* and *Cryptococcus* show that copper promotes the generation of reactive oxygen species (ROS), which lead to oxidative stress, damaging cellular components like membranes and proteins. Moreover, it has been shown that in *C. neoformans*, Cu induces a proteomic response that down-regulates protein synthesis while up-regulating protein degradation pathways, ultimately inhibiting fungal growth [56].

3.5. Cytotoxicity assay

The *in vitro* biocompatibility assessment of pristine and Cu-loaded HA NPs was performed to confirm the well-established cytocompatibility of HA derivates and to evaluate the Cu-induced proliferative or cytocidal effects on VERO cell line. The VERO cell line is a widely used cytological model for assessing adaptability of novel compounds and surfaces in a mammalian and human context. A cytotoxic effect (defined as a viability percentage lower than 70% compared to growth control, according to ISO 10993-5:2009) on this cell line usually indicates significant challenges for biomedical research advancement of tested compound/material.

Cytotoxicity evaluation was performed after 24 h of co-incubation between NPs and VERO cells. The tested concentrations of the NPs range from 8 to 128 μg/ml, which correspond to the antifungal concentrations determined with broth microdilution method. The NPs tested are pristine HA, representing the least effective in antimicrobial terms, but serving as the control to assess HA cytocompatibility regardless of copper loading, and HA-Cu-0.1, which is the most effective antifungal NPs tested and has the highest copper loading. Previous studies on HA NPs have described a copper dose-dependent cytotoxic effect, with a viability percentage around 75% after 24 h [57,58].

As shown in Fig. 5, pristine HA has a very solid viability percentage compared to control, with no dose-dependency: all tested concentrations range from 100 to 106% viability, and a proliferative effect is observed at 128 μg/mL, with 114% viability. These results agree with previous studies which assessed the cytotoxicity of silver doped hydroxyapatites [59]. Conversely, the copper content in HA-Cu-0.1 seems to impact VERO cells viability in a tolerable manner. The higher concentrations tested (256 and 128 μg/mL) show viability percentage of 71 and 72%, respectively, which are slightly above the cytotoxicity cut-off of 70% viability compared to growth control. From 64 to 8 μg/mL there is an inverse proportionality between Ha-Cu-0.1 concentration and VERO viability, indicating a dose-dependent relationship between the copper loaded NPs and cytocompatibility. Finally, the lowest concentration

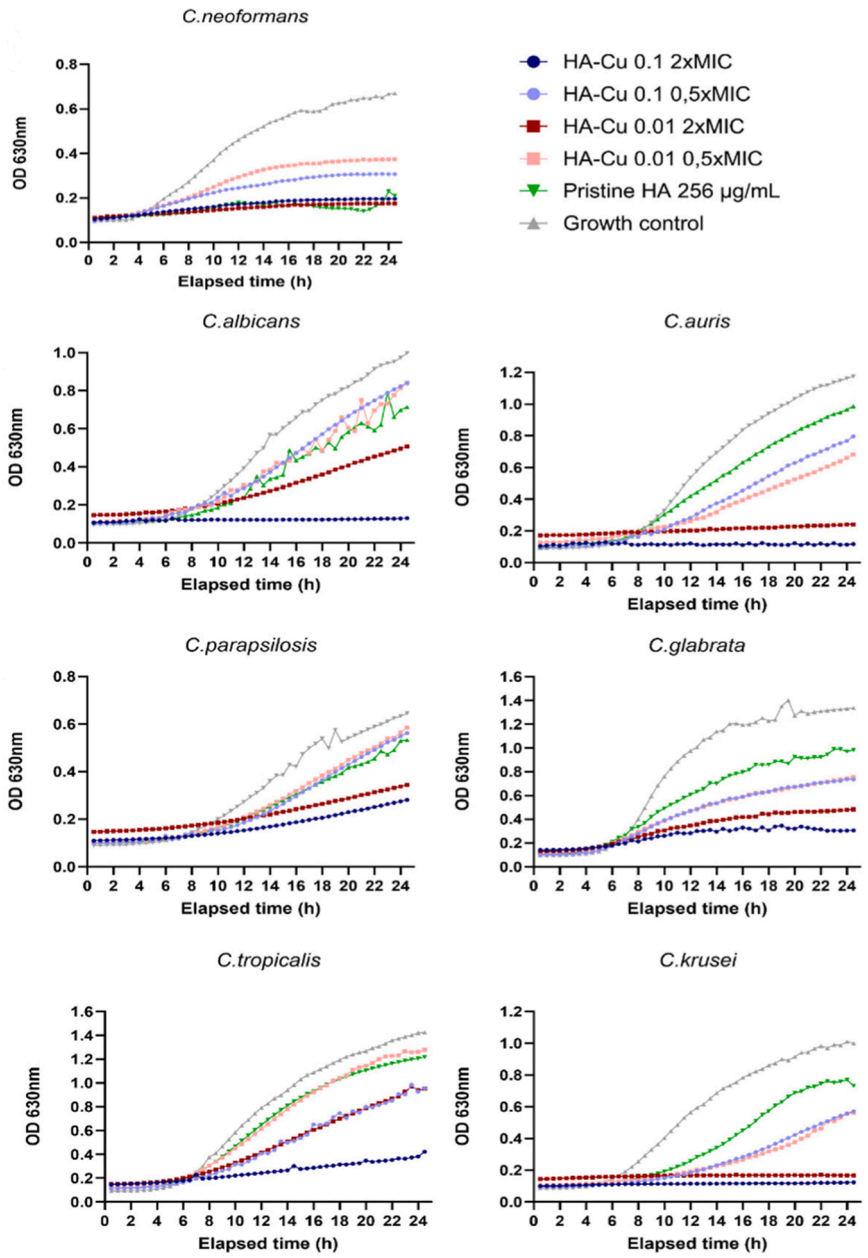

Fig. 4. Growth curves of *Candida albicans, Candida auris, Candida parapsilosis, Candida glabrata, Candida tropicalis, Candida krusei* and *Cryptococcus neoformans* in the presence of HA-Cu-0.1 and HA-Cu-0.01 at double (2 × MIC) and half (0.5 × MIC) minimum inhibitory concentrations, and pristine HA at higher concentration tested (256 µg/mL), compared to the growth control. Each data point represents an optical density reading taken every 30 min over a period of 24 h. Raw data with errors, also expressed in colony forming unit per milliliter (CFU/mL), are reported in the Supplementary Materials (Tables S1–14).

tested, 8 µg/mL, show 105 % viability, indicating a total absence of cytotoxicity.

4. Conclusions

In this study we synthesized P-rich HA with a Ca/P ratio of 1.48, characterized by nanometric size (BET SSA *ca.* 200 m^2/g). As evidenced by the TEM images, the nanoparticles show a morphology elongated in the direction of the crystallographic *c*-axis and by XRD analysis average crystalline domains sizes of 13.2 ± 0.5 nm along the [200] direction and 4.4 ± 0.7 nm along the [310] direction were obtained. The samples were functionalized with copper through ion exchange. NPs physico-chemical properties were preserved after functionalization except for the samples treated with 0.2 M Cu^{2+} solution which, due to its low pH, induced a partial dissolution of the HA particles. Rietveld refinement of the XRD patterns highlighted a small contraction of the cell parameters upon Cu doping. The copper content gradually increased reaching a maximum value of 14 %wt. Our findings indicate that copper functionalization occurs through different mechanisms: at lower concentrations, the (Ca+Cu)/P ratio of the pristine material (1.48) is maintained suggesting a Ca^{2+} -> Cu^{2+} ionic exchange, while at higher concentrations (*i.e.* Cu > 10 %wt) additional mechanisms such as surface complexation are involved. Surface active sites were probed by FTIR of adsorbed carbon monoxide evidencing the presence of both Ca and Cu cations even for the high-copper content HA-Cu-0.1 sample.

Regarding the antifungal activity, HA-Cu-0.1 and HA-Cu-0.05 samples exhibited promising performances with low minimum inhibitory concentrations (MIC < 64 µg/mL) against critical pathogens including drug-resistant strains *C. auris* and *Cryptococcus* species, which pose significant challenges to global health, especially among

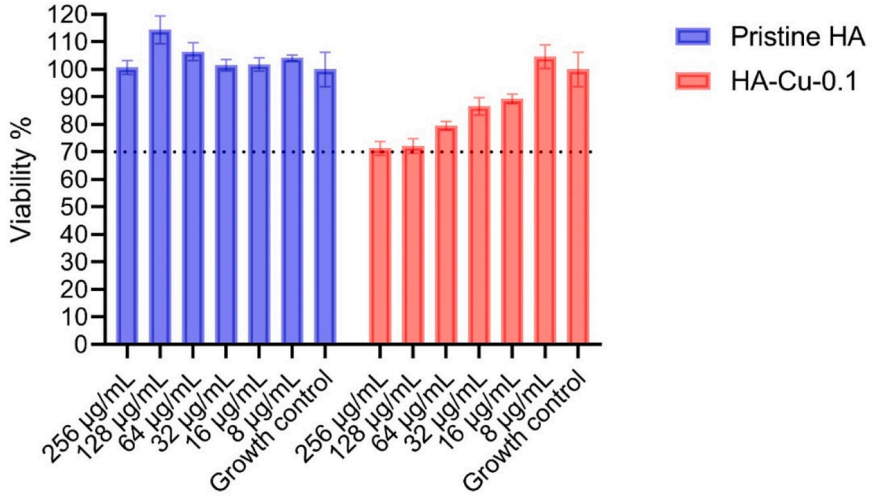

Fig. 5. Viability percentages of VERO cell line after 24 h, expressed as relative fraction of growth control, for pristine HA (blue) and HA-Cu-0.1 (red). The horizontal dotted black line highlights the viability cut-off for biological cytotoxicity.

immunocompromised patients. Unique kinetic responses were observed, particularly in reducing optical density for *C. neoformans*. *Candida* species within the NCAC group, such as *C. parapsilosis*, exhibited varying degrees of resistance to compounds tested. Notably, HA-Cu and pristine HA displayed significant inhibitory effects on specific species such as *C. krusei*, which is inherently resistant to azole-based drugs but show susceptibility to HA-Cu in a dose-dependent manner.

Cytotoxicity evaluation on VERO cell line revealed adequate biocompatibility of both undoped and Cu-doped HA. A decrease in cell viability was observed for Cu-doped HA when tested at high concentrations (256 and 128 µg/mL), compared to pristine HA. However, the cytotoxic effect on mammalian cells was less pronounced at concentrations effective against yeast growth, suggesting a potential for targeted antifungal action.

In summary, our findings provide insights into the potential of copper-doped HAs as effective antifungal agents, offering an alternative for therapeutic approaches against diverse *Candida* and *Cryptococcus* infections.

CRediT authorship contribution statement

Guillermo Escolano-Casado: Writing – original draft, Visualization, Investigation, Data curation. **Camilla Fusacchia:** Investigation. **Lorenzo Degli Esposti:** Investigation. **Margherita Cacaci:** Investigation. **Damiano Squitieri:** Writing – review & editing, Visualization, Investigation. **Francesca Bugli:** Supervision, Conceptualization. **Michele Iafisco:** Writing – review & editing, Supervision, Conceptualization. **Lorenzo Mino:** Writing – original draft, Supervision, Conceptualization.

Declaration of competing interest

The authors declare that they have no known competing financial interests or personal relationships that could have appeared to influence the work reported in this paper.

Acknowledgments

F.B. and M.I. acknowledge the Italian Ministry of University and Research (MUR) (Project "CHANCE" PRIN 2022, Research Grant 2022CCN7WM, founded by the European Union—Next Generation EU) for providing financial support to this work. L.M. acknowledges support from the Project CH4.0 under the MUR program "Dipartimenti di Eccellenza 2023–2027'' (project code: D13C22003520001) and from the PRIN Project PERFECT (project code: P2022TK9B9). C.F. acknowledges the Italian Ministry of University and Research (Project funded under the National Recovery and Resilience Plan (NRRP), funded by the European Union - NextGenerationEU - Mission 4 Component 1 Investment 3.3 - Call for tender No. 117 of 02/03/2023).

Supplementary materials

Supplementary material associated with this article can be found, in the online version, at doi:10.1016/j.surfin.2025.106179.

Data availability

Data will be made available on request.

References

[1] S.V. Dorozhkin, Calcium orthophosphates, J. Mater. Sci. 42 (2007) 1061–1095, https://doi.org/10.1007/s10853-006-1467-8.
[2] S.V. Dorozhkin, Nanodimensional and nanocrystalline apatites and other calcium orthophosphates in biomedical engineering, Biol. Med. Mater. 2 (2009) 1975–2045, https://doi.org/10.3390/ma2041975.
[3] M. Sadat-Shojai, M.T. Khorasani, E. Dinpanah-Khoshdargi, A. Jamshidi, Synthesis methods for nanosized hydroxyapatite with diverse structures, Acta Biomater. 9 (2013) 7591–7621, https://doi.org/10.1016/j.actbio.2013.04.012.
[4] R.O. Kareem, N. Bulut, O. Kaygili, Hydroxyapatite biomaterials: a comprehensive review of their properties, structures, medical applications, and fabrication methods, J. Chem. Rev. 6 (2024) 1–26, https://doi.org/10.48309/jcr.2024.415051.1253.
[5] A. Fihri, C. Len, R.S. Varma, A. Solhy, Hydroxyapatite: a review of syntheses, structure and applications in heterogeneous catalysis, Coord. Chem. Rev. 347 (2017) 48–76, https://doi.org/10.1016/j.ccr.2017.06.009.
[6] J. Gomez-Morales, M. Iafisco, J.M. Delgado-Lopez, S. Sarda, C. Drouet, Progress on the preparation of nanocrystalline apatites and surface characterization: overview of fundamental and applied aspects, Prog. Cryst. Growth Charact. Mater. 59 (2013) 1–46, https://doi.org/10.1016/j.pcrysgrow.2012.11.001.
[7] F. Chiatti, M. Corno, Y. Sakhno, G. Martra, P. Ugliengo, Revealing hydroxyapatite nanoparticle surface structure by CO adsorption: a combined B3LYP and infrared study, J. Phys. Chem. C 117 (2013) 25526–25534, https://doi.org/10.1021/jp4086574.
[8] Y. Sakhno, P. Ivanchenko, M. Iafisco, A. Tampieri, G. Martra, A step toward control of the surface structure of biomimetic hydroxyapatite nanoparticles: effect of carboxylates on the {010} P-Rich/Ca-Rich facets ratio, J. Phys. Chem. C 119 (2015) 5928–5937, https://doi.org/10.1021/jp510492m.
[9] C.A. Ospina, J. Terra, A.J. Ramirez, M. Farina, D.E. Ellis, A.M. Rossi, Experimental evidence and structural modeling of nonstoichiometric (010) surfaces coexisting in hydroxyapatite nano-crystals, Colloid Surf. B-Biointerfaces 89 (2012) 15–22, https://doi.org/10.1016/j.colsurfb.2011.08.016.
[10] L. Bertinetti, A. Tampieri, E. Landi, C. Ducati, P.A. Midgley, S. Coluccia, G. Martra, Surface structure, hydration, and cationic sites of nanohydroxyapatite: UHR-TEM, IR, and microgravimetric studies, J. Phys. Chem. C 111 (2007) 4027–4035, https://doi.org/10.1021/jp066040s.
[11] S. Campisi, C. Castellano, A. Gervasini, Tailoring the structural and morphological properties of hydroxyapatite materials to enhance the capture efficiency towards

copper(ii) and lead(ii) ions, New J. Chem. 42 (2018) 4520–4530, https://doi.org/10.1039/c8nj00468d.
[12] S. Campisi, M.G. Galloni, F. Bossola, A. Gervasini, Comparative performance of copper and iron functionalized hydroxyapatite catalysts in NH_3-SCR, Catal. Commun. 123 (2019) 79–85, https://doi.org/10.1016/j.catcom.2019.02.008.
[13] C. Drouet, M.T. Carayon, C. Combes, C. Rey, Surface enrichment of biomimetic apatites with biologically-active ions Mg^{2+} and Sr^{2+}: a preamble to the activation of bone repair materials, Mater. Sci. Eng. C-Biomimetic Supramol. Syst. 28 (2008) 1544–1550, https://doi.org/10.1016/j.msec.2008.04.011.
[14] C. Rey, C. Combes, C. Drouet, H. Sfihi, A. Barroug, Physico-chemical properties of nanocrystalline apatites: implications for biominerals and biomaterials, Mater. Sci. Eng. C-Biomimetic Supramol. Syst. 27 (2007) 198–205, https://doi.org/10.1016/j.msec.2006.05.015.
[15] M. Gruselle, Apatites: a new family of catalysts in organic synthesis, J. Organomet. Chem. 793 (2015) 93–101, https://doi.org/10.1016/j.jorganchem.2015.01.018.
[16] P. Ivanchenko, G. Escolano-Casado, L. Mino, L. Dassi, J.F. Fernandez-Sánchez, G. Martra, J. Gómez-Morales, Structural and surface studies of luminescent Ca/Eu phosphate nanomaterials: from the bulk to surface features, Colloid Surf. B-Biointerfaces 217 (2022) 7, https://doi.org/10.1016/j.colsurfb.2022.112620.
[17] R.A. Hajjeh, A.N. Sofair, L.H. Harrison, G.M. Lyon, B.A. Arthington-Skaggs, S. A. Mirza, M. Phelan, J. Morgan, W. Lee-Yang, M.A. Ciblak, L.E. Benjamin, L. T. Sanza, S. Huie, S.F. Yeo, M.E. Brandt, D.W. Warnock, Incidence of bloodstream infections due to Candida species and in vitro susceptibilities of isolates collected from 1998 to 2000 in a population-based active surveillance program, J. Clin. Microbiol. 42 (2004) 1519–1527, https://doi.org/10.1128/JCM.42.4.1519-1527.2004.
[18] K. Satoh, K. Makimura, Y. Hasumi, Y. Nishiyama, K. Uchida, H. Yamaguchi, Candida auris sp. nov., a novel ascomycetous yeast isolated from the external ear canal of an inpatient in a Japanese hospital, Microbiol. Immunol. 53 (2009) 41–44, https://doi.org/10.1111/j.1348-0421.2008.00083.x.
[19] H. Du, J. Bing, T. Hu, C.L. Ennis, C.J. Nobile, G. Huang, Candida auris: epidemiology, biology, antifungal resistance, and virulence, PLoS Pathog. 16 (2020), https://doi.org/10.1371/journal.ppat.1008921.
[20] H. Sati, A. Alastruey-Izquierdo, J. Perfect, N.P. Govender, T.S. Harrison, T. Chiller, T.C. Sorrell, F. Bongomin, R. Oladele, A. Chakrabarti, R. Wahyuningsih, A. L. Colombo, J.L. Rodriguez-Tudela, C. Beyrer, N. Ford, HIV and fungal priority pathogens, Lancet HIV 10 (2023) e750–e754, https://doi.org/10.1016/S2352-3018(23)00174-1.
[21] M.M. Canuto, F. Gutierrez, Antifungal drug resistance to azoles and polyenes, Lancet Infect. Dis. 2 (2002) 550–563, https://doi.org/10.1016/s1473-3099(02)00371-7.
[22] N.M. Revie, K.R. Lyer, N. Robbins, L.E. Cowen, Antifungal drug resistance: evolution, mechanisms and impact, Curr. Opin. Microbiol. 45 (2018) 70–76, https://doi.org/10.1016/j.mib.2018.02.005.
[23] C. Giannini, V. Holy, L. De Caro, L. Mino, C. Lamberti, Watching nanomaterials with X-ray eyes: probing different length scales by combining scattering with spectroscopy, Prog. Mater. Sci. 112 (2020), https://doi.org/10.1016/j.pmatsci.2020.100667.
[24] C. Velino, F. Carella, A. Adamiano, M. Sanguinetti, A. Vitali, D. Catalucci, F. Bugli, M. Iafisco, Nanomedicine approaches for the pulmonary treatment of cystic fibrosis, 7 (2019). https://doi.org/10.3389/fbioe.2019.00406.
[25] T. Huang, X. Li, M. Maier, N.M. O'Brien-Simpson, D.E. Heath, A.J. O'Connor, Using inorganic nanoparticles to fight fungal infections in the antimicrobial resistant era, 158 (2023) 56–79. https://doi.org/10.1016/j.actbio.2023.01.019.
[26] L.E. Garcia-Marin, K. Juarez-Moreno, A.R. Vilchis-Nestor, E. Castro-Longoria, Highly antifungal activity of biosynthesized copper oxide nanoparticles against Candida albicans, Nanomaterials 12 (2022), https://doi.org/10.3390/nano12213856.
[27] V. Stanić, S. Dimitrijević, J. Antić-Stanković, M. Mitrić, B. Jokić, I.B. Plećaš, S. Raičević, Synthesis, characterization and antimicrobial activity of copper and zinc-doped hydroxyapatite nanopowders, Appl. Surf. Sci. 256 (2010) 6083–6089, https://doi.org/10.1016/j.apsusc.2010.03.124.
[28] W. Zakrzewski, M. Dobrzynski, J. Nowicka, M. Pajaczkowska, M. Szymonowicz, S. Targonska, P. Sobierajska, K. Wiglusz, W. Dobrzynski, A. Lubojanski, S. Fedorowicz, Z. Rybak, R.J. Wiglusz, The influence of ozonated olive oil-loaded and copper-doped nanohydroxyapatites on planktonic forms of microorganisms, Nanomaterials 10 (2020) 1–21, https://doi.org/10.3390/nano10101997.
[29] A. Mengistu, M. Naimuddin, B. Abebe, Optically amended biosynthesized crystalline copper-doped ZnO for enhanced antibacterial activity, RSC Adv. 13 (2023) 24835–24845, https://doi.org/10.1039/d3ra04488b.
[30] Y. Ohsumi, K. Kitamoto, Y. Anraku, Changes induced in the permeability barrier of the yeast plasma membrane by cupric ion, J. Bacteriol. 170 (1988) 2676–2682, https://doi.org/10.1128/jb.170.6.2676-2682.1988.
[31] E.W. Hunsaker, K.J. Franz, Copper potentiates azole antifungal activity in a way that does not involve complex formation, Dalton Trans. 48 (2019) 9654–9662, https://doi.org/10.1039/c9dt00642g.
[32] I. Khemiri, F. Tebbji, A. Sellam, Transcriptome analysis uncovers a link between copper metabolism, and both fungal fitness and antifungal sensitivity in the opportunistic yeast Candida albicans, Front. Microbiol. 11 (2020) 935, https://doi.org/10.3389/fmicb.2020.00935.
[33] S. Shanmugam, B. Gopal, Copper substituted hydroxyapatite and fluorapatite: synthesis, characterization and antimicrobial properties, Ceram. Int. 40 (2014) 15655–15662, https://doi.org/10.1016/j.ceramint.2014.07.086.
[34] T. Tite, A.C. Popa, L.M. Balescu, I.M. Bogdan, I. Pasuk, J.M.F. Ferreira, G.E. Stan, Cationic substitutions in hydroxyapatite: current status of the derived biofunctional effects and their in vitro interrogation methods, Materials 11 (2018) 62, https://doi.org/10.3390/ma11112081.
[35] E. Battiston, L. Antonielli, S. Di Marco, F. Fontaine, L. Mugnai, Innovative delivery of Cu(II) ions by a nanostructured hydroxyapatite: potential application in planta to enhance the sustainable control of *Plasmopara viticola*, Phytopathology 109 (2019) 748–759, https://doi.org/10.1094/phyto-02-18-0033-r.
[36] V. Mondello, O. Fernandez, J.-F. Guise, P. Trotel-Aziz, F. Fontaine, In planta activity of the novel copper product HA + Cu(II) based on a biocompatible drug delivery system on vine physiology and trials for the control of botryosphaeria dieback, Front. Plant Sci. 12 (2021), https://doi.org/10.3389/fpls.2021.693995.
[37] B. Gottardo, T.H. Lemes, G. Byzynski, M.H. Paziani, M.R. von-Zeska-Kress, M.T. G. de Almeida, D.P. Volanti, One-pot synthesis and antifungal activity of nontoxic silver-loaded hydroxyapatite nanocomposites against *Candida* Species, ACS Appl. Nano Mater. 2 (2019) 2112–2120, https://doi.org/10.1021/acsanm.9b00091.
[38] C.A. Zamperini, R.S. André, V.M. Longo, E.G. Mima, C.E. Vergani, A.L. Machado, J. A. Varela, E. Longo, Antifungal applications of Ag-decorated hydroxyapatite nanoparticles, J. Nanomater. 2013 (2013) 9, https://doi.org/10.1155/2013/174398.
[39] C.S. Ciobanu, M.V. Predoi, N. Buton, C. Megier, S.L. Iconaru, D. Predoi, Physicochemical characterization of europium-doped hydroxyapatite thin films with antifungal activity, Coatings 12 (2022) 16, https://doi.org/10.3390/coatings12030306.
[40] C.S. Turculet, A.M. Prodan, I. Negoi, G. Teleanu, M. Popa, E. Andronescu, M. Beuran, G.A. Stanciu, R. Hristu, M.L. Badea, A. Iosif, S.M. Raita, N. Vineticu, R. Trusca, O. Lupescu, Preliminary evaluation of the antifungal activity of samarium doped hydroxyapatite thin films, Rom. Biotech. Lett. 23 (2018) 13927–13932, https://doi.org/10.26327/rbl2018.220.
[41] G. Escolano-Casado, P. Ivanchenko, G. Paul, C. Bisio, L. Marchese, A.M. Ashrafi, V. Milosavljevic, L. Degli Esposti, M. Iafisco, L. Mino, Surface and structural characterization of Cu-exchanged hydroxyapatites and their application in H_2O_2 electrocatalytic reduction, Appl. Surf. Sci. 595 (2022) 153495, https://doi.org/10.1016/j.apsusc.2022.153495.
[42] S. Koutsopoulos, E. Dalas, Hydroxyapatite crystallization in the presence of serine, tyrosine and hydroxyproline amino acids with polar side groups, J. Cryst. Growth 216 (2000) 443–449, https://doi.org/10.1016/s0022-0248(00)00415-2.
[43] WHO fungal priority pathogens list to guide research, 2022, ISBN 978-92-4-006024-1.
[44] The European Committee on Antimicrobial Susceptibility Testing - Antifungal susceptibility testing (AFST), 2020. Clinical breakpoints for fungi v. 10.0.
[45] L. Mino, G. Spoto, S. Bordiga, A. Zecchina, Rutile surface properties beyond the single crystal approach: new insights from the experimental investigation of different polycrystalline samples and periodic DFT calculations, J. Phys. Chem. C 117 (2013) 11186–11196, https://doi.org/10.1021/jp401916q.
[46] J. Jemal, H. Tounsi, K. Chaari, C. Petitto, G. Delahay, S. Djemel, A. Ghorbel, NO reduction with NH_3 under oxidizing atmosphere on copper loaded hydroxyapatite, Appl. Catal. B-Environ. 113 (2012) 255–260, https://doi.org/10.1016/j.apcatb.2011.11.045.
[47] Y. Sakhno, L. Bertinetti, M. Iafisco, A. Tampieri, N. Roveri, G. Martra, Surface hydration and cationic sites of nanohydroxyapatites with amorphous or crystalline surfaces: a comparative study, J. Phys. Chem. C 114 (2010) 16640–16648, https://doi.org/10.1021/jp105971s.
[48] C.S. Ciobanu, D. Predoi, S.L. Iconaru, M.V. Predoi, L. Ghegoiu, N. Buton, M. Motelica-Heino, Copper doped hydroxyapatite nanocomposite thin films: synthesis, physico–chemical and biological evaluation, BioMetals (2024), https://doi.org/10.1007/s10534-024-00620-2.
[49] J.M. Delgado-López, M. Iafisco, I. Rodríguez, A. Tampieri, M. Prat, J. Gómez-Morales, Crystallization of bioinspired citrate-functionalized nanoapatite with tailored carbonate content, Acta Biomater. 8 (2012) 3491–3499, https://doi.org/10.1016/j.actbio.2012.04.046.
[50] C. Jäger, T. Welzel, W. Meyer-Zaika, M. Epple, A solid-state NMR investigation of the structure of nanocrystalline hydroxyapatite, Magn. Reson. Chem. 44 (2006) 573–580, https://doi.org/10.1002/mrc.1774.
[51] K. Hadjiivanov, H. Knozinger, FTIR study of CO and NO adsorption and coadsorption on a Cu/SiO_2 catalyst: probing the oxidation state of copper, Phys. Chem. Chem. Phys. 3 (2001) 1132–1137, https://doi.org/10.1039/b009649k.
[52] S. Pantaleone, F. Pellegrino, V. Maurino, M. Corno, P. Ugliengo, L. Mino, Disclosing the true atomic structure of {001} facets in shape-engineered TiO_2 anatase nanoparticles, J. Mater. Chem. A 12 (2024) 4325–4332, https://doi.org/10.1039/d3ta06694k.
[53] J. Schumann, J. Krohnert, E. Frei, R. Schlogl, A. Trunschke, IR-spectroscopic study on the interface of Cu-based methanol synthesis catalysts: evidence for the formation of a ZnO overlayer, Top. Catal. 60 (2017) 1735–1743, https://doi.org/10.1007/s11244-017-0850-9.
[54] K.E. Pristov, M.A. Ghannoum, Resistance of Candida to azoles and echinocandins worldwide, Clin. Microbiol. Infect. 25 (2019) 792–798, https://doi.org/10.1016/j.cmi.2019.03.028.
[55] H.O. Khalifa, V. Hubka, A. Watanabe, M. Nagi, Y. Miyazaki, T. Yaguchi, K. Kamei, Prevalence of antifungal resistance, genetic basis of acquired Azole and Echinocandin resistance, and genotyping of Candida krusei recovered from an international collection, Antimicrob. Agents Chemother. 66 (2022) e01856, https://doi.org/10.1128/AAC.01856-21. -01821.
[56] T. Sun, Y. Li, Y. Li, H. Li, Y. Gong, J. Wu, Y. Ning, C. Ding, Y. Xu, Proteomic analysis of copper toxicity in human fungal pathogen cryptococcus neoformans, Front. Cell. Infect. Microbiol. 11 (2021), https://doi.org/10.3389/fcimb.2021.662404.

[57] S.I. Korowash, Z. Keskin-Erdogan, B.A. Hemdan, L.V. Barrios Silva, D.M. Ibrahim, D.Y.S. Chau, Selenium- and/or copper-substituted hydroxyapatite: a bioceramic substrate for biomedical applications, J. Biomater. Appl. 38 (2023) 351–360, https://doi.org/10.1177/08853282231198726.
[58] K.M. Weiss, S.K. Kucko, S. Mokhtari, T.J. Keenan, A.W. Wren, Investigating the structure, solubility, and antibacterial properties of silver- and copper-doped hydroxyapatite, J. Biomed. Mater. Res. Part B Appl. Biomater. 111 (2023) 295–313, https://doi.org/10.1002/jbm.b.35151.
[59] D. Predoi, S.L. Iconaru, M.V. Predoi, Bioceramic layers with antifungal properties, Coatings 8 (2018), https://doi.org/10.3390/coatings8080276.